Available online at www.sciencedirect.com
ScienceDirect
International Journal of Heat and Mass Transfer 50 (2007) 2571–2581
International Journal of HEAT and MASS TRANSFER
www.elsevier.com/locate/ijhmt

Boundary conditions at the solid–liquid surface over the multiscale channel size from nanometer to micron

Jinliang Xu [a,*], Yuxiu Li [a,b]

[a] Micro Energy System Laboratory, Guangzhou Institute of Energy Conversion, Chinese Academy of Science, Nengyuan Road, Wushan, Guangzhou 510640, PR China
[b] Graduate School of Chinese Academy of Science, CAS, Beijing 100039, PR China

Received 1 September 2006; received in revised form 8 November 2006
Available online 20 February 2007

Abstract

The boundary condition at the solid surface is one of the important problems for the microfluidics. In this paper we study the effects of the channel sizes on the boundary conditions (BC), using the hybrid computation scheme adjoining the molecular dynamics (MD) simulations and the continuum fluid mechanics. We could reproduce the three types of boundary conditions (slip, no-slip and locking) over the multiscale channel sizes. The slip lengths are found to be mainly dependent on the interfacial parameters with the fixed apparent shear rate. The channel size has little effects on the slip lengths if the size is above a critical value within a couple of tens of molecular diameters. We explore the liquid particle distributions nearest the solid walls and found that the slip boundary condition always corresponds to the uniform liquid particle distributions parallel to the solid walls, while the no-slip or locking boundary conditions correspond to the ordered liquid structures close to the solid walls.

The slip, no-slip and locking interfacial parameters yield the positive, zero and negative slip lengths respectively. The three types of boundary conditions existing in "microscale" still occur in "macroscale". However, the slip lengths weakly dependent on the channel sizes yield the real shear rates and the slip velocity relative to the solid wall traveling speed approaching those with the no-slip boundary condition when the channel size is larger than thousands of liquid molecular diameters for all of the three types of interfacial parameters, leading to the quasi-no-slip boundary conditions.

Keywords: Boundary condition; Slip length; Interfacial parameter; Channel size

1. Introduction

The boundary condition is one of the important basic problems in fluid flow and heat transfer. The widely used no-slip boundary condition indicates that the liquid particles adjacent to the solid walls are stationary relative to the solid when liquid flows over a solid surface. People use the no-slip boundary condition to reproduce many macroscopic experiments for hundreds of years. However, it is being received challenge when the channel size is down to micron and nanometer, with the fast development of the microfluidic and nanofluidic devices in recent years. The mechanism by which liquids transport mass, momentum and energy should be different from that for gases [1]. Applying shear stress across the channels yields the motion of the liquid particles with relative layers. The dense nature of liquids precludes the use of kinetic theory of gases [1]. The present paper focuses on the analysis of liquid flows in microchannels.

Even though numerous studies on the boundary conditions in small scales can be found in literatures, the general conclusions are far to reach at this stage. The slip lengths are reported to be varied from 20 nm to 1 μm [2]. A lot of factors influence the boundary conditions in small

* Corresponding author. Tel./fax: +86 20 87057656.
E-mail address: xujl@ms.giec.ac.cn (J. Xu).

0017-9310/$ - see front matter © 2007 Elsevier Ltd. All rights reserved.
doi:10.1016/j.ijheatmasstransfer.2006.11.031

Nomenclature

c_1	non-dimensional parameter, $c_1 = \rho_w/\rho$
c_2	non-dimensional parameter, $c_2 = \varepsilon_{wf}/\varepsilon$
c_3	non-dimensional parameter, $c_3 = \sigma_{wf}/\sigma$
E	square root error between the MD simulations and the hybrid computations
F_{ext}	external force on the top surface of the P domain received from $z > L_{cp}$
F_{ij}	intermolecular force between a pair of liquid atoms
F_{ij_w}	intermolecular force between a pair of liquid and solid atoms
k_B	Boltzmann's constant
L	length of a unit lattice cell
L_x, L_y	lengths of the computational ensemble of the Couette flow in x and y coordinates
L_z	half channel height of the Couette flow geometry
L_{cp}	distance between the bottom solid wall and the top surface of the P domain
L_s	slip length
L_{pc}	distance between the bottom solid wall and the center plane of the $p \to c$ layer
m	mass of a single liquid argon atom
n	the number of data points
N	liquid atom number in the P domain
N_{cp}	liquid atom number in the $c \to p$ layer
N_w	solid wall atoms involved in the MD computation
PR	spatial distribution of liquid argon atoms nearest the solid wall
r	distance between a pair of atoms
x, y, z	three coordinates
t	time
T_B	bulk liquid temperature
u	axial velocity
u_f	liquid velocity on the solid wall surface
u_i^{hc}	axial velocity by the hybrid computations for the ith data point
u_i^{MD}	axial velocity by the MD simulations for the ith data point
$u_{p\to c}$	axial velocity at $z = L_{pc}$ decided by the parameter averaging
u_s	slip velocity, $u_s = u_w - u_f$
u_w	solid wall traveling velocity
ε	energy scale between a pair of liquid argon atoms
ε_{wf}	energy scale between a pair of argon and solid atoms
ϕ	potential
γ_a	apparent shear rate, $\gamma_a = u_w/L_z$
γ_r	real shear rate determined by the slope line of the velocity profile at $z = L_z$
$\tilde{\eta}$	Gaussian distributed random force with zero mean and variance of $2mk_BT_B\Gamma$
λ	the criterion number governing the boundary conditions, $\lambda = c_1^{1/3}c_3$
μ	viscosity
ρ	argon atom number per unit volume
ρ_w	solid atom number per unit volume
σ	length scale between a pair of liquid atoms
σ_{wf}	length scale between a pair of liquid and solid atoms
τ	characteristic time of argon atom
$\tilde{\tau}$	shear stress over the xy plane
Δx, Δy	grid lengths over a single unit lattice cell in x and y directions
Δt	time step for the MD simulations
Δz	a single bin thickness in z direction
Δz_{cp}	the thickness of the $c \to p$ layer
Δz_{pc}	the thickness of the $p \to c$ layer
Γ	friction constant that controls the rate of heat exchange between the fluids and reservoir

scales, including the solid–liquid interactions [3–5], the surface wettability [6–9], the surface roughness [10–12], the nucleation of nanobubbles on the solid surface [13–15] and the system temperatures [16], etc.

The widely used MD simulation is an effective tool to study the boundary condition in nanoscale [3,4,8,11,17–20]. It is well known that the MD simulations cost a large quantity of computation resource, which significantly limits the channel size that can be dealt with. Most of the above cited numerical works are performed for the channel size in the order of 10 nm.

Alternatively, the slip lengths and the velocity profiles in small scales can be determined by the experimental measurements. The newly fast development of the micro-particle-image velocimetry (μ-PIV) is available for such measurements [7]. However, the characteristic size of the microchannels should be at least 10 μm for the experimental measurements at this stage.

Thus a large gap exists for the channel characteristic sizes that can be treated between the MD simulations and the experimental measurements. Less is known on the size dependent slip lengths in the public literatures. The questions are those at what size does the slip boundary condition begins to occur and how to distinguish the "micro" and "macro" from the physics point of view? This is the motivation of the present paper.

We consider the Couette flow sheared by the two solid walls, which are traveling at constant speed in opposite directions. The slip lengths and the macroscopic velocity profiles are determined by the hybrid computation scheme, which divides the computation domain into a molecular dynamics domain (the P domain), a continuum fluid

mechanics domain (the C domain) and an overlap domain. The important solid–liquid surface interactions were considered in the P domain. Using such a tool we can reproduce the three types of boundary conditions with the channel height from nanometer to micron by selecting the interfacial parameters based on our newly developed three-atom-model and the criterion number [5]. We found that the slip lengths are weakly dependent on the channel sizes when the sizes are above a critical value within a couple of tens of molecular diameters. We explore the liquid particle distributions nearest the solid walls and found that there is a strong connection among the interfacial parameters, the slip lengths and the liquid particle distributions close to the solid walls.

Finally we describe the important deductions from the weakly dependent slip length over the channel sizes. The real shear rates and the slip velocity relative to the solid wall traveling speed approach those with the no-slip boundary conditions when the channel characteristic sizes are larger than thousands of liquid molecular diameters. To the authors' knowledge, the channel size dependent boundary conditions were not reported previously.

2. The Couette flow geometry and domain decomposition

Before we describe the hybrid computation scheme, we give the assumptions that were made for the Couette flow.

- The liquid argon ($\rho\sigma^3 = 0.805$) with the well-known Lennard-Jones potential is used.
- The two solid walls are smooth and the solid atoms are arranged based on the face-central-cubic (fcc) structure. They are traveling at constant speed in opposite directions, in between the liquid argon is filled.
- The intermolecular force interactions are not only considered among liquid argon particles, but also between the argon and the solid atoms. The solid–liquid interactions have the similar potentials as those among the liquid particles, leading to three interfacial parameters given later.
- The present study fixes the non-dimensional apparent shear rate of $\gamma_a\tau = 0.05$, γ_a and τ are the apparent shear rate and the characteristic time of the argon. The previous studies [16,21] shows that the apparent shear rates do not affect the boundary conditions if they are less than a critical value. $\gamma_a\tau = 0.05$ is less than such critical transition value.

The non-dimensional shear rates of $\gamma_a\tau$ in the literatures [16,21] are usually in the range from 0.01 to 0.1. Considering $\tau = 2.16 \times 10^{-12}$ s, the above range corresponds to the shear rates of γ_a in the range from 4.63×10^9 s^{-1} to 4.63×10^8 s^{-1}. The present paper uses $\gamma_a\tau = 0.05$, corresponding to $\gamma_a = 2.31 \times 10^8$ s^{-1}.

Due to the exact geometry symmetry of the Couette flow, Fig. 1 only shows one half of the computation domain below the central plane. The three-dimensional coordinates are attached.

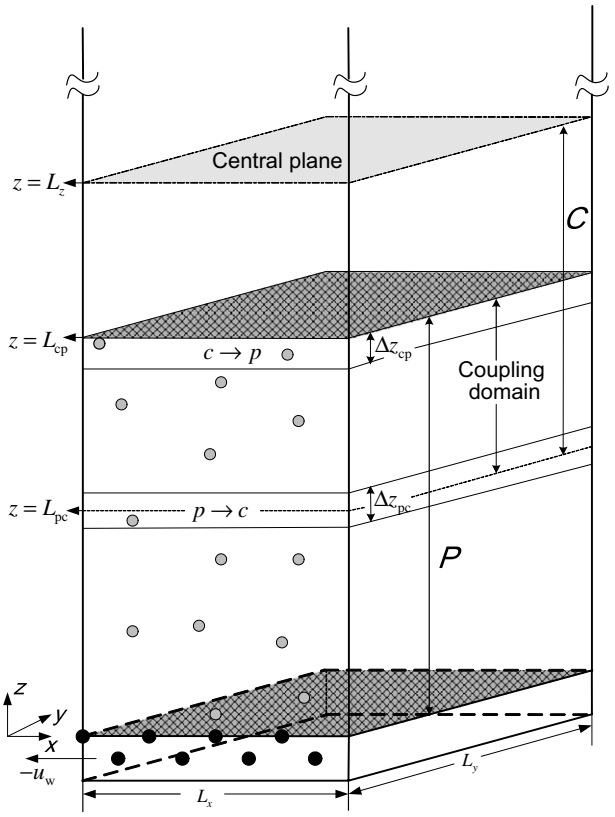

Fig. 1. The Couette flow geometry and the domain decomposition.

The domain decomposition is needed for the hybrid computation. Three sub-domains were created: the molecular dynamics domain (P domain, $0 < z < L_{cp} = 17.85\sigma$), the C domain ($L_{pc} = 7.79\sigma < z < L_z$), and the coupling domain ($L_{pc} < z < L_{cp}$). There are two thin liquid layers for the exchange fluxes of mass, momentum and energy, between the two classical computations: $p \to c$ and $c \to p$ layers. The $p \to c$ layer has the thickness of Δz_{pc}, equals to a bin thickness for the parameter averaging in the MD computations. The thickness of the $c \to p$ layer equals to $\Delta z_{cp} = 2.5\sigma$. L_x and L_y are 10.22σ over the entire computation domain.

3. The hybrid computational scheme for the Couette flow

The hybrid computation scheme is being developed to link the atomic scale and the macroscale in recent years. Several research groups [22–24] are developing the hybrid method. The literature survey can be found in Koumoutaskos [24]. The scheme employs the MD close to the walls where the molecular effects are important. Theoretically only a very thin layered fluid which has the thickness larger than several times of the cut-off distance of 2.5σ needs to be considered due to the short range intermolecular force behavior among particles. The reminder region was treated by the continuum fluid mechanics. An overlap region is set

in which both the MD and the continuum fluid mechanics are considered. The mass, momentum and energy exchanges take place there. A general consideration of the mass, momentum and energy exchanges was analyzed by Delgado-Buscalioni and Coveney [23]. The primary advantage of the hybrid computation is to reduce the computation time for a large molecular number system. Besides, the method could significantly extend the computation domain that the pure MD simulations cannot deal with.

3.1. Molecular dynamics simulation

The MD simulation was performed in the P domain regarding Fig. 1, involving the treatment of the solid wall atoms and the liquid particles. Outside of the Couette flow geometry the periodic boundary conditions are applied in x and y coordinates, but the periodic boundary condition does not exist in z direction.

Several layers of the bottom solid wall atoms are involved in the MD simulation. These solid atoms are selected based on the criterion that the distance between the liquid atoms at the solid–liquid surface and the solid atoms of the outer solid layer should be at least $2.5\sigma_{\mathrm{wf}} = 2.5c_3\sigma$.

Applying the Newton's second law, the acceleration of the argon atom i is expressed as

$$m\frac{\mathrm{d}^2\vec{r}}{\mathrm{d}t^2} = \sum_{j\neq i,j=1}^{N}\vec{F}_{ij} + \sum_{j_{\mathrm{w}}=1}^{N_{\mathrm{w}}}\vec{F}_{ij_{\mathrm{w}}} \tag{1}$$

Note that the first term of the right side of Eq. (1) represents the intermolecular force among liquid particles, and the second term of the right side of Eq. (1) is the intermolecular force between the liquid atom i and the solid particles.

Because the P domain ends at $z = L_{cp}$, Eq. (1) is only suitable for $0 \leqslant z \leqslant L_{cp} - \Delta z_{cp}$. Actually $c \to p$ layer is the top boundary of the P domain. When the Newton's second law is applied in the $c \to p$ layer, an additional external force from $z > L_{cp}$ should be included. Besides, the bottom solid wall is quite far away from the $c \to p$ layer, the intermolecular force between the liquid atom in the $c \to p$ layer and the solid particles can be neglected. Thus the Newton's second law is written for the liquid particle in the $c \to p$ layer as

$$m\frac{\mathrm{d}^2\vec{r}}{\mathrm{d}t^2} = \sum_{j\neq i,j=1}^{N}\vec{F}_{ij} + F_{\mathrm{ext}}/N_{cp} \tag{2}$$

F_{ext} is the total external force from $z > L_{cp}$ and N_{cp} is the liquid atom number in the $c \to p$ layer. The determination of F_{ext} will be given later.

The solid particles are arranged as the fcc structure during the whole computation process. Thus the solid temperatures are assumed to be zero. Such treatment is similar to those used in the previous studies [3–5,17,21]. At the beginning of the MD simulation, the initial conditions are given for the liquid particle positions, velocities and high order derivatives. The liquid positions are also based on the fcc structure. However, the liquid particles will significantly deviate from the fcc structure after the MD simulation was performed. The random initial velocities of the liquid atoms are assumed, but scaled using the liquid temperature of $T_{\mathrm{B}} = 1.2\varepsilon/k_{\mathrm{B}}$. The initial liquid accelerations are determined in terms of the positions of $r_i(0)$ by computing the force on each liquid particle and applying the Newton's second law. The initial zero of high order derivatives will be updated following the MD simulations.

At each time step, the fifth-order Gear finite-difference algorithm was used to acquire the numerical results, consisting of the predict step and the correction step. The characteristic time of argon is $\tau = (m\sigma^2/\varepsilon)^{0.5}$. The time step is chosen in the range of $\Delta t = 0.005$–0.0005τ, depending on the BCs. For the no-slip or locking BCs, $\Delta t = 0.005\tau$ is small enough. For the slip BCs, a more shorter time step is needed.

Shearing the liquids by the two solid walls leads to the viscous dissipation which warms up the liquid system. In order to maintain the liquid temperature as the desired value, we introduce the damping and Langevin noise terms in v_y. Such technique is similar to that used by Thompson and Troian [17]. The resulting equation in y coordinate becomes

$$m\ddot{y}_i = \sum_{j\neq i,j=1}^{N}F_{ij,y} + \sum_{j_{\mathrm{w}}=1}^{N_{\mathrm{w}}}F_{ij_{\mathrm{w}},y} - m\Gamma\dot{y}_i + \tilde{\eta}_i \tag{3}$$

where Γ is a friction constant that controls the rate of heat exchange with the thermal bath reservoir. $\tilde{\eta}$ is a Gaussian distributed random force with zero mean and variance of $2mk_{\mathrm{B}}T_{\mathrm{B}}\Gamma$. The third and fourth terms of the right side of Eq. (3) are the damping and noise terms respectively. Because the y component is perpendicular to the shear plane, using the damping and noise terms in the y component can successfully remove the heat produced by the viscous heat dissipation.

The important macroscopic parameters include the velocities, temperatures and non-dimensional number densities. These parameters are stable after the initial time elapsed, such as 150τ. In order to acquire the macroscopic parameters, a set of bins are divided in the P domain, which are parallel to the xy plane. Each liquid bin has the thickness of $\Delta z = 0.425\sigma$. The numerical integrations were performed for these bins, yielding the velocity profile across the P domain.

We compute the spatial distribution $PR(x, y)$ of liquid atoms parallel to the xy plane for the first, second and third bins nearest the solid walls. In each liquid bin, a set of lattice cells in the xy plane are divided. The four corners and the center of the lattice cell exactly match the positions of the corresponding solid wall atoms in the xy plane. The next step is to divide the single unit lattice cell into a set of grids on the xy plane. Totally there are 24×24 grids

divided for a single unit lattice cell, with each grid of $\Delta x = \Delta y = L/24$, in which L is the length of a single unit lattice cell. The liquid atoms that fall into each grid are counted. Such counting process was performed over 150τ after the initial 150τ elapsed.

3.2. The hybrid computation scheme

The hybrid scheme links the MD simulations with the continuum fluid mechanics. The most important procedure is to deal with the mass, momentum and energy exchanges in the $c \to p$ and $p \to c$ layers (see Fig. 1).

The $p \to c$ coupling: Regarding Fig. 1, remember that the center plane of the Couette flow has the zero mean axial velocity due to the geometry symmetry. The continuum fluid mechanics simulation in the C domain needs a boundary condition of the mean axial velocity at $z = L_{pc}$, which is coming from the $p \to c$ coupling. Assuming that we have the mean axial velocity $u_{p\to c}$ at $z = L_{pc}$ which is derived from the parameter averaging based on the MD simulations, the linear velocity profiles over the C domain can be written as follows:

$$u = -\frac{u_{p\to c}}{L_z - L_{pc}}(z - L_z) \tag{4}$$

Note that the linear velocity profile in the C domain is ensured because the interface at $z = L_{pc}$ is so "far" that the solid wall particles have no effect on the liquid atoms in the C domain.

The $c \to p$ coupling: The MD simulations treated the bottom boundary by computing the intermolecular force interactions between the liquid and solid atoms. We note that the MD simulations lack another boundary condition at $z = L_{cp}$, which can be from the $c \to p$ coupling.

Giving Eq. (4), the shear stress at the interface of $z = L_{cp}$ can be derived as

$$\tilde{\tau} = \mu\frac{\partial u}{\partial z} = -\mu\frac{u_{p\to c}}{L_z - L_{pc}} \tag{5}$$

The total shear force at the interface of $z = L_{cp}$ is

$$F_{\text{ext}} = \tilde{\tau}L_xL_y = -\mu\frac{u_{p\to c}}{L_z - L_{pc}}L_xL_y \tag{6}$$

Regarding the liquid argon, the previous studies [17,21] show that the viscosity μ follows $\mu/\varepsilon\tau\sigma^{-3} = 2.0$. We assume that such external force is applied uniformly on each liquid atom within the layer of $c \to p$, thus F_{ext}/N_{cp} is the external force term in Eq. (2), yielding the closure relation for the MD simulation over the entire P domain.

An important issue is that the liquid atoms inside the P domain can escape out of the P domain from the interface of $z = L_{cp}$, leading to the decreased number densities in the P domain. An effective method to keep the constant or quasi-constant liquid particle numbers is to insert the corresponding liquid atoms in the P domain, which is described in Delgado-Buscalioni and Coveney [25].

3.3. The iterative procedure of the hybrid computation scheme

Fig. 2 shows the iterative process of the hybrid computation scheme. For most of the runs, the entire integration

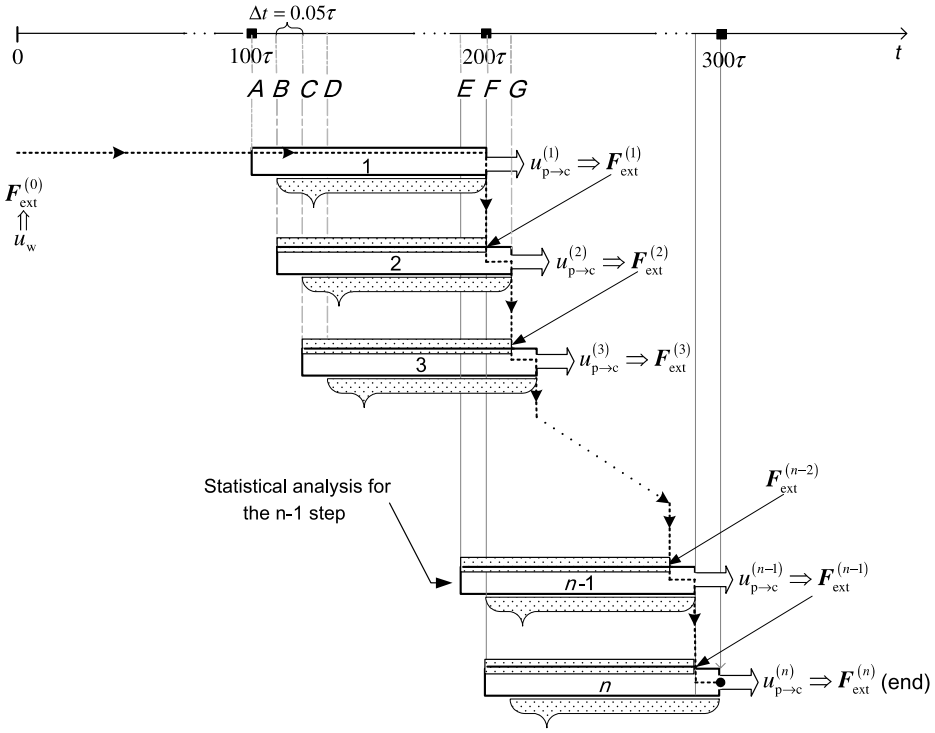

Fig. 2. The iterative process of the hybrid computation scheme.

time is 300τ. Each newly updated macroscopic parameters, such as velocities, temperatures and liquid number densities, are averaged over 100τ for each iterative step, indicated by the white rectangular frame. There are two systems involved in the iterative process. The first one is the MD simulation versus time, represented by the dashed line with array. The second system shows the parameter averaging process, followed by the momentum exchanges in the $p \to c$ and $c \to p$ layers. They were performed at the end of each rectangular frame. The newly obtained external force applied in the $c \to p$ layer forms the updated boundary condition so that the MD simulation can be successively continued.

Initially at $t = 0$, most of the initial conditions and boundary conditions are described for the P domain above except the $c \to p$ layer. Because at this time the macroscopic flow field was not established, we assume the no-slip BC at the bottom solid–liquid surface, leading to the linear mean axial velocity profile against the half channel height from u_w at $z = 0$ to $u = 0$ at $z = L_z$, in terms of which, the external force applied in the $c \to p$ region from $z > L_{cp}$ is

$$F_{ext}^{(0)} = \mu u_w L_x L_y / L_z \tag{7}$$

Eq. (7) is used as the top BC for the MD simulations until at $t = 200\tau$.

The first macroscopic parameters are averaged from 100τ to 200τ, leading to $u_{p\to c}^{(1)}$. With the newly updated mean axial velocity of $u_{p\to c}^{(1)}$, the external force $F_{ext}^{(1)}$ is obtained over the $c \to p$ layer using Eqs. (4)–(6), forming the updated top boundary condition for the MD simulation over the entire P domain.

For the general consideration, the ith iterative step moves forward 0.05τ succeeded from the $(i-1)$th iterative step. The macroscopic parameters are averaged over the time span from $[100 + (i-1) \times 0.05]\tau$ to $[200 + (i-1) \times 0.05]\tau$, yielding $u_{p\to c}^{(i)}$. The momentum exchange in the $p \to c$ and $c \to p$ layers by Eqs. (4)–(6) finally results in $F_{ext}^{(i)}$, forming the new top boundary condition for the MD simulation in the entire C domain.

The iterative process repeats until at the end of 300τ. The integration time is verified so that the macroscopic parameters did not change at all with further increasing the integration time.

4. Results and discussion

4.1. Validation of the hybrid computation scheme

We note that in Eqs. (1) and (2), $F_{ij} = -\partial\phi_{ij}/\partial r_{ij}$ and $F_{ij_w} = -\partial\phi_{ij_w}/\partial r_{ij_w}$. The well-known Lennard-Jones potential is used among the argon atoms: $\phi_{ij} = 4\varepsilon\left[\left(\frac{\sigma}{r}\right)^{12} - \left(\frac{\sigma}{r}\right)^{12}\right]$. Besides, we use the similar potential between the argon and solid atoms as that among argon atoms, but use ε_{wf} and σ_{wf} to replace ε and σ instead. At the solid interface, there are three parameters involved in the force integration: the density ratio $c_1 = \rho_w/\rho$, the energy scale ratio $c_2 = \varepsilon_{wf}/\varepsilon$, and the length scale ratio $c_3 = \sigma_{wf}/\sigma$. In our previous study [5], we developed a new non-dimensional criterion number that governs the boundary conditions, $\lambda = c_1^{1/3} c_3$, based on a newly developed three-atom-model. Thus the three governing interfacial parameters become two: λ and c_2. The two microsystems would have the same boundary conditions if they have the same two parameters. When λ approaches 0.757, the no-slip or locking boundary conditions occur (depending on c_2). However, if λ deviates from 0.757, the slip flow occurs. Always, increasing c_2 yields the decreased slip degree, or enhanced the locking degree. Thus, we use three groups of the interfacial parameters in the present paper

$$\left.\begin{array}{lll} c_1 = 1.0, & c_2 = 0.2, & c_3 = 0.3 \\ c_1 = 1.0, & c_2 = 1.0, & c_3 = 0.7 \\ c_1 = 1.0, & c_2 = 4.0, & c_3 = 0.76 \end{array}\right\} \tag{8}$$

The above parameters correspond to

$$\left.\begin{array}{ll} \lambda = 0.3, & c_2 = 0.2 \\ \lambda = 0.7, & c_2 = 1.0 \\ \lambda = 0.76, & c_2 = 4.0 \end{array}\right\} \tag{9}$$

for the slip, no-slip and locking boundary conditions respectively. Thus we name the above three groups of the parameters as the slip, no-slip and locking interfacial parameters, respectively.

The pure MD simulation results were used as the benchmark data to verify the hybrid computation scheme. Because the MD simulation is limited by the channel size, the entire channel height of the Couette flow geometry is $2L_z = 51.8\sigma$ for the MD simulation, with both top and bottom solid walls considered. However, the hybrid computation scheme only needs to consider the half channel height of 25.9σ due to the geometry symmetry at $z = L_z$. Fig. 3 shows the comparisons of the velocity profile between the

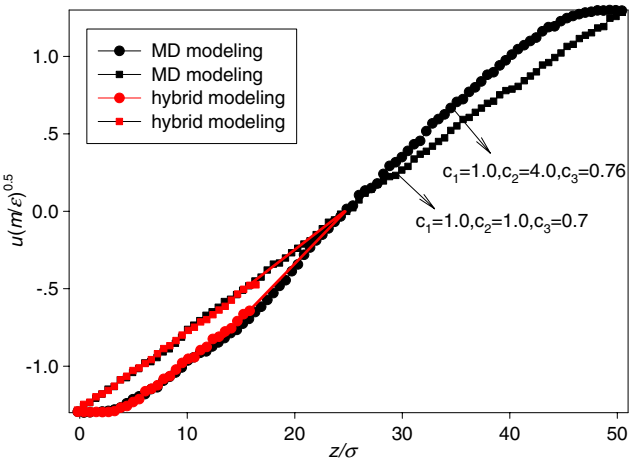

Fig. 3. Comparisons of the velocity profiles between the hybrid computations and the pure MD simulations for the Couette flow with the no-slip and locking boundary conditions.

MD simulations and the hybrid computation for the no-slip ($c_1 = 1.0, c_2 = 1.0, c_3 = 0.7$) and locking ($c_1 = 1.0$, $c_2 = 4.0, c_3 = 0.76$) interfacial parameters. As shown in Fig. 3, the no-slip interfacial parameters cause the linear velocity profile across the entire channel height by the MD simulation, which is successfully reproduced by the hybrid computation scheme. They coincide with each other for the mean velocity profiles. For the locking BC, both simulations show the curved velocity distribution near the solid walls followed by a straight line distribution and they coincide with each.

In order to identify their differences quantitatively, the square root errors are acquired which is based on the following computations:

$$E = \sqrt{\frac{\sum_{i=1}^{n}\left(\frac{u_i^{\mathrm{hc}} - u_i^{\mathrm{MD}}}{u_i^{\mathrm{MD}}}\right)^2}{n}} \tag{10}$$

where n is the data points involved in the computations, u_i^{hc} is the mean axial velocity by the hybrid computation simulation and u_i^{MD} is the mean axial velocity by the MD simulations. A pair of u_i^{hc} and u_i^{MD} share the same z coordinates. The square root errors are 2.45% and 2.70% for the no-slip and locking boundary conditions respectively.

Due to the available computational resource, most of previous MD simulations can only consider the channel size in the order of 10 nm. This is why we develop the hybrid computation scheme to study the channel size effect on the boundary conditions in the present paper.

4.2. The slip lengths weakly dependent on the channel size from nano to micron

Fig. 4 shows the mean axial velocity profile across the half channel height for the slip and locking BC interfacial parameters with $L_z = 800\sigma$. The data points are only available in the P domain. The linear velocity distribution followed by the P domain is predicted by Eq. (4). For the slip interfacial parameter, a perfect linear velocity profile is observed across the entire half channel height (see Fig. 4a), with $u_{\mathrm{w}}(m/\varepsilon)^{0.5} = 40.043$ and $u_{\mathrm{s}}(m/\varepsilon)^{0.5} = 1.434$. For the locking BC, a curved velocity distribution is observed close to the solid wall, followed by the linear distribution. The slope at $z = L_z$ determined slip length is $L_{\mathrm{s}} = -5.75\sigma$. Compared with the previous studies by the MD simulations at "small" length scale [3–5,17], "large" channel size does not change the shape of the velocity profile for both of the slip and locking BCs.

We plotted the slip lengths in Fig. 5 for the three interfacial parameters given in Eqs. (8) and (9) with L_z from 5σ to 3000σ, corresponding to 1.7 nm to 1.022 μm. We found that the slip lengths are slightly higher as the channel size L_z is less than 10σ for the slip and locking interfacial parameters. The previous studies such as Din and Michaelides [26] also show that the channel sizes have effect on the slip lengths with small channel sizes. Under such condition the liquid particles have the oscillation distributions near the solid walls and inhomogeneities will appear in the fluid. However, the slip lengths are very weakly dependent on the channel size for all of the three interfacial parameters once L_z is larger than a couple of tens σ.

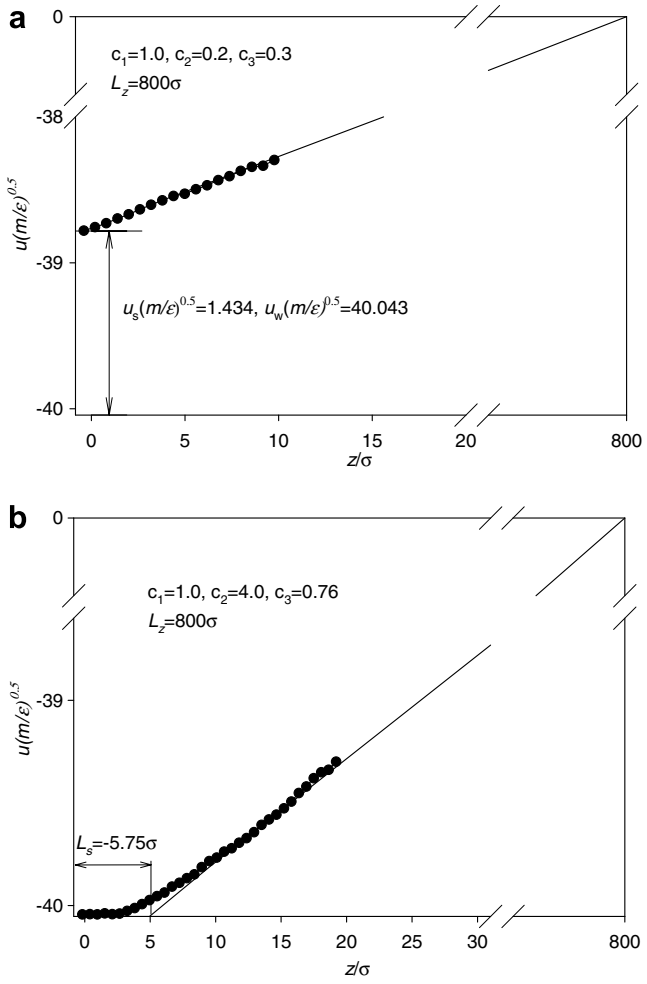

Fig. 4. The mean velocity profiles across the half channel height with $L_z = 800\sigma$.

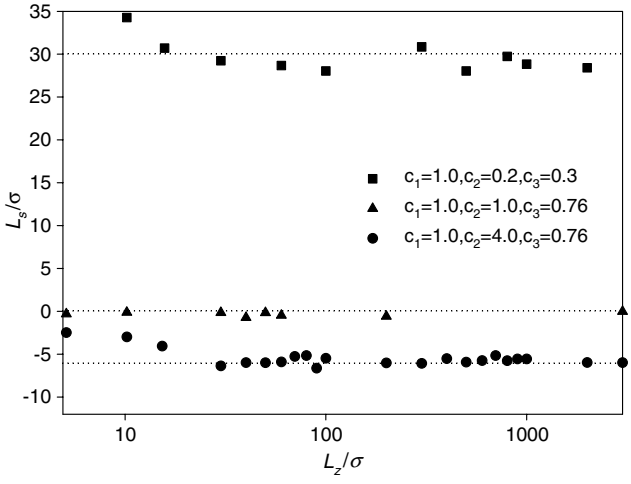

Fig. 5. The weakly dependent slip lengths versus the channel size for the three typical interfacial parameters if $L_z > 10\sigma$.

As shown in Fig. 5, a perfect zero slip length is obtained for the no-slip interfacial parameter of $\lambda = 0.7, c_2 = 1.0$ with L_z from nano to micron. Similarly, the slip interfacial parameter of $\lambda = 0.3, c_2 = 0.2$ induces the slip length of $29.7\sigma = 10.12$ nm and the locking interfacial parameter of $\lambda = 0.76, c_2 = 4.0$ results in the slip length of $-5.7\sigma = -1.94$ nm when $L_z > 10\sigma$.

4.3. Fluid structure parallel to walls

The channel sizes have little effect on the slip lengths with the fixed interfacial parameters if $L_z > 10\sigma$. We found that there is a strong connection between the interfacial parameters and the liquid particle distributions nearest the solid walls.

We plot the PR distribution nearest the solid walls with two different L_z of 30σ and 800σ in Fig. 6. We did find that the PR distribution is very similar for both of the two channel sizes for a specific group of interfacial parameter. The slip interfacial parameter of $\lambda = 0.3, c_2 = 0.2$ yields the quasi-uniform PR distribution, corresponding to the slip BC, for both of the two channel sizes (see Fig. 6a and b). When λ is increased to $\lambda = 0.7$ and $c_2 = 1.0$, the ordered structure of the first liquid layer nearest the solid walls begin to occur, displaying very similar distribution for the two channel sizes (see Fig. 6c and d). With the critical

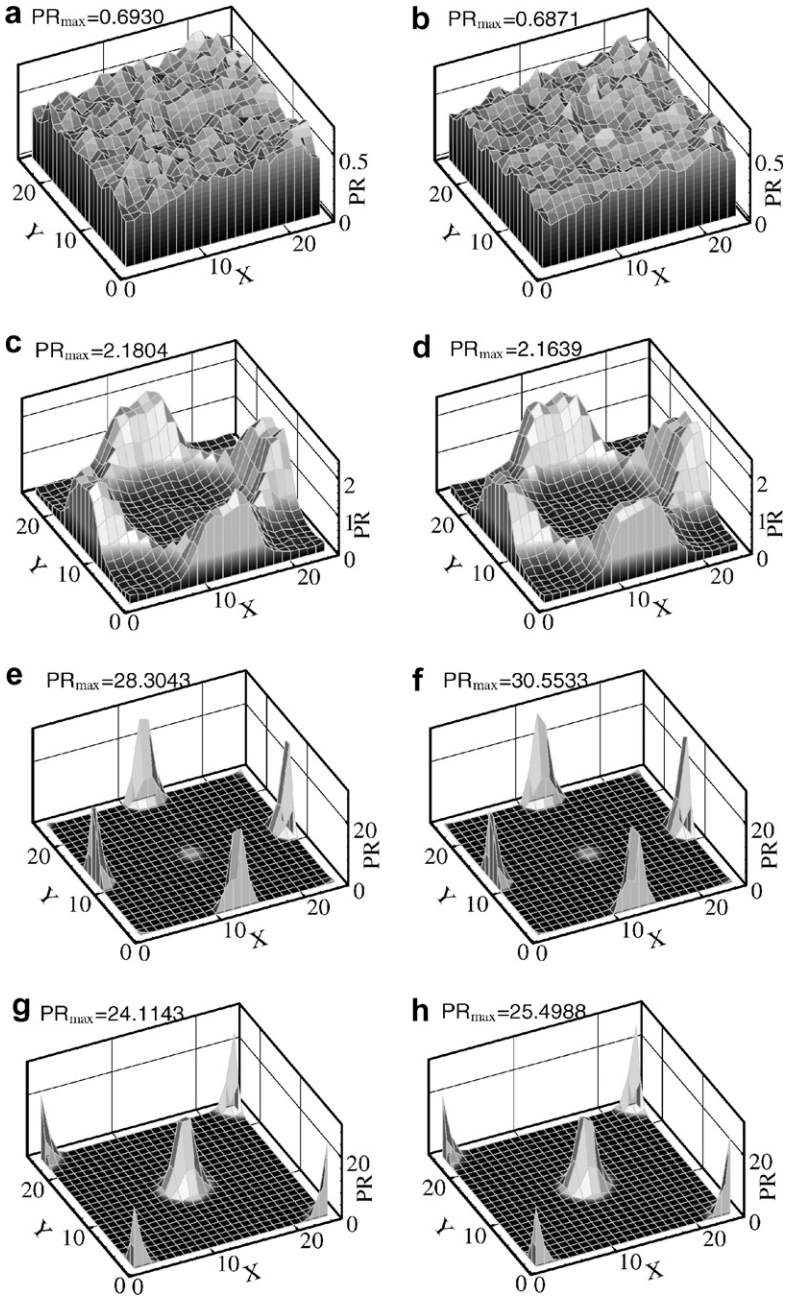

Fig. 6. The comparison of the PR distribution with $L_z = 30\sigma$ and $L_z = 800\sigma$ (left column for $L_z = 30\sigma$ and right column for $L_z = 800\sigma$, (a, b) $\lambda = 0.3, c_2 = 0.2$, (c, d) $\lambda = 0.7, c_2 = 1.0$, (e–h) $\lambda = 0.76, c_2 = 4.0$, (e, f) for the first layer, (g, h) for the second layer).

criterion number of $\lambda = 0.76$ and higher c_2 of 4.0, the extended fcc structure of the first and second liquid layers nearest the solid walls occur (see Fig. 6e–h). We name this phenomenon as the epitaxial order structure. The very similar PR distributions of the liquid particles nearest the solid walls yield the similar slip lengths with the varied channel size. In other words, the channel sizes do not change the liquid particle distributions nearest the solid walls, leading to the slip lengths weakly dependent on the multiscale channel size if $L_z > 10\sigma$.

4.4. The slip velocity relative to the solid wall speed and the real shear rate versus the channel size

It is noted that the slip length characterizes the boundary conditions, physically. We identified that the slip lengths are mainly relied on the interfacial parameters but weakly dependent on the multichannel sizes if $L_z > 10\sigma$. Now we analyze the boundary conditions from an angle that is different from that of the slip length. We present the ratio of the slip velocity on the solid surface to the solid wall speed (u_s/u_w), and the real shear rate (γ_r) versus the channel size.

Generally the velocity profiles for the slip and locking boundary conditions are shown in Fig. 7. The exact no-slip boundary condition is a transition case from the slip flow to the locking flow. The point O is on the solid surface while the point A is on the centerline of the Couute flow geometry. In Fig. 7a, the line OA is the assumed velocity profile with the exact no-slip boundary condition, thus γ_a is named as the apparent shear rate. The line AB is the real velocity profile. Thus "OAB" is named as the velocity triangle. The slope line of the velocity profile at $z = L_z$ determines the real shear rate of γ_r. Extension of the slope line at $z = L_z$ with the z coordinate yields the D point. The slip length L_s is represented by DO. The slip velocity u_s is defined as the velocity difference between the solid wall and the liquid on the surface, which can be represented by OB.

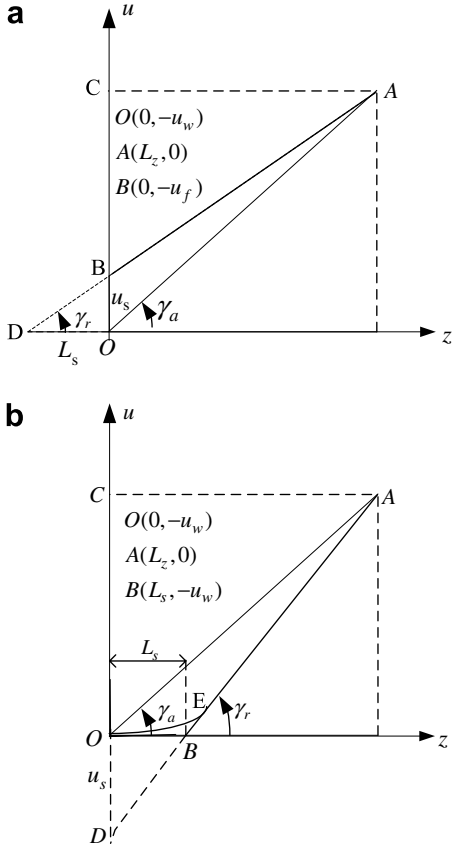

Fig. 7. The velocity triangles for the slip and locking boundary conditions.

Fig. 7b shows the velocity triangle for the locking BCs. Again the line OA is the assumed velocity profile with the exact no-slip BCs. The real velocity profile is OEA, consisting of two parts, one is the curved part close to the solid walls of OE, and the straight part of EA. The slope line at $z = L_z$ (the line AED) determines L_s and u_s. It should be noted that the liquids at the solid walls exactly reach the traveling velocity of the solid walls, leading to the zero slip velocity at the solid walls, physically, which is against the slope line determined u_s. But the slope line determined u_s is an important parameter to characterize the flow deviating from the classical solution with the no-slip BCs. Both of L_s and u_s are negative for the locking BCs.

Regarding Fig. 7, u_s and γ_r have the following simple expressions:

$$u_s = \frac{L_z L_s}{L_z + L_s}\gamma_a \tag{11}$$

$$\gamma_r = \frac{L_z}{L_z + L_s}\gamma_a \tag{12}$$

γ_r is the slope of the velocity profile at $z = L_z$, indicating the real shear rate.

We plotted $\gamma_r\tau$ and u_s/u_w against L_z/σ for the three typical interfacial parameters in Fig. 8. The no-slip interfacial parameter yields $\gamma_r \approx \gamma_a$ and $u_s \approx 0$ with $5\sigma \leqslant L_z \leqslant 3000\sigma$. For the slip interfacial parameter of $\lambda = 0.3, c_2 = 0.2$, the non-dimensional real shear rates of $\gamma_r\tau$ are smaller than the non-dimensional apparent shear rate of $\gamma_a\tau = 0.05$ but they are increased with increasing L_z. Meanwhile the slip velocity relative to the solid speed of u_s/u_w is decreased with increasing L_z. Both of $\gamma_r\tau$ and u_s/u_w approach those for the no-slip solutions when $L_z > 1000\sigma$.

The locking interfacial parameter of $\lambda = 0.76, c_2 = 4.0$ yields the higher real shear rates than the apparent value but they are decreased with increasing L_z. The negative u_s/u_w is increased with increasing L_z. Similar to the Couette flow for the slip interfacial parameter, $\gamma_r\tau$ and u_s/u_w approach those for the no-slip BCs when $L_z > 1000\sigma$.

The above finding provides us an important clue to understand the boundary condition. Physically there is no transition from "micro" to "macro". The slip lengths are mainly dependent on the interfacial parameters with little effect of the channel sizes as long as $L_z > 10\sigma$. Depending on the interfacial parameters, the three types of boundary

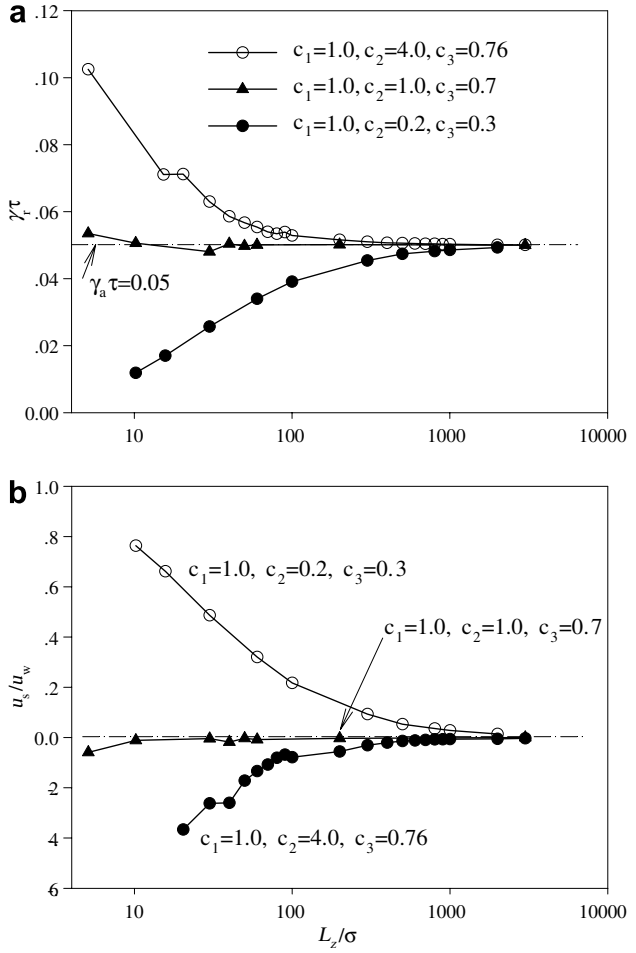

Fig. 8. The real shear rates and slip velocities relative to the solid wall speed versus the channel size by the hybrid computations.

conditions existing in "microscale" still occur in "macroscale". *This is the absoluteness of the boundary conditions.* However, the real shear rates and the slip velocity relative to the solid wall speed approach those with the no-slip boundary condition when the channel characteristic size is larger than thousands of molecular diameters for all of the three types of the interfacial parameters, leading to the quasi-no-slip boundary conditions. *This is the relativity of the boundary conditions.*

Again, we note that the above conclusion is valid with the assumption of the smooth solid wall surface and the fixed system temperature. Effects of these factors on the boundary conditions over the multiscale channel sizes are expected in the future.

5. Conclusions

The major conclusions that were drawn in the present paper are summarized as follows:

- We developed the hybrid computation scheme for the Couette flow to study the boundary conditions and velocity profiles in the Couette flow geometries. We select the three typical interfacial parameters: the slip, no-slip and locking interfacial parameters to characterize the Couette flow.
- It is found that the slip lengths are mainly dependent on the interfacial parameters, weakly dependent on the channel size as long as such size is larger than a couple of tens of molecular diameters. The slip, no-slip and locking interfacial parameters yield the positive, zero and negative slip lengths, respectively.
- There is a strong connection among the interfacial parameters, the liquid particle distributions nearest the solid walls and the slip lengths. The slip interfacial parameters always cause the quasi-uniform liquid distributions nearest the solid walls, leading to the slip flow. When the criterion number approaches the critical value of 0.747, the ordered liquid structure for the first liquid layer begins to occur, corresponding to the zero slip length. The locking interfacial parameters yield the extended fcc liquid particle distributions for the first and second layers nearest the solid walls, corresponding to the negative slip length. The channel sizes have little effect on this connection.
- Physically there is no any transition from "micro" to "macro". Depending on the interfacial parameters, the three types of boundary conditions existing in "microscale" still occur in "macroscale", indicated by the weakly dependent slip lengths on the channel sizes. *This is the absoluteness of the boundary conditions.* However, the real shear rates and the slip velocity relative to the solid wall speed approach those with the no-slip boundary conditions when the channel size is larger than thousands of liquid molecular diameters for all of the three interfacial parameters, leading to the quasi-no-slip boundary conditions. *This is the relativity of the boundary conditions.*

Acknowledgements

The work is supported by the National Basic Research Program with the contract number 2006CB601203, and the Natural Science Foundation of China with the contract numbers 10272102 and 50476088.

References

[1] M. Gad-el-Hak, Gas and liquid transport at the microscale, Heat Transfer Eng. 27 (4) (2006) 13–29.
[2] C.H. Choi, K. Johan, A. Westin, K.S. Breuer, Apparent slip flows in hydrophilic and hydrophobic microchannels, Phys. Fluids 15 (10) (2003) 2897–2902.
[3] P.A. Thompson, M.O. Robbins, Simulations of contact-line motion: slip and the dynamics contact angle, Phys. Rev. Lett. 63 (7) (1989) 766–769.
[4] P.A. Thompson, M.O. Robbins, Shear flow near solids: epitaxial order and flow boundary conditions, Phys. Rev. A 41 (12) (1990) 6830–6837.
[5] Y.X. Li, J.L. Xu, A new criterion number for the boundary conditions at the solid–liquid interface in nanoscale, Nanoscale Microscale Thermophys. Eng. 10 (2) (2006) 109–141.

[6] J. Baudry, E. Charlaix, A. Tonck, D. Mazuyer, Experimental evidence for a large slip effect at a nonwetting fluid–solid interface, Langmuir 17 (17) (2001) 5232–5236.
[7] D.C. Tretheway, C.D. Meinhart, Apparent fluid slip at hydrophobic microchannel walls, Phys. Fluids 14 (3) (2002) L9–L12.
[8] G. Nagayama, P. Cheng, Effects of interface wettability on microscale flow by molecular dynamics simulation, Int. J. Heat Mass Transfer 47 (3) (2004) 501–513.
[9] C. Cottin-Bizonne, B. Cross, A. Steinberger, E. Charlaix, Boundary slip on smooth hydrophobic surfaces: intrinsic effects and possible artifacts, Phys. Rev. Lett. 9405 (5) (2005) 6102.
[10] K. Watanabe, Y. Udagawa, Drag reduction of Newtonian fluid in a circular pipe with a highly water-repellant wall, J. Fluid Mech. 381 (1999) 225–238.
[11] A. Jabbarzadeh, J.D. Atkinson, R.I. Tanner, Effects of the wall roughness on slip and rheological properties of hexadecane in molecular dynamics simulation of Couette shear flow between two sinusoidal walls, Phys. Rev. E 61 (1) (2000) 690–699.
[12] E. Bonaccurso, H.J. Butt, V.S.J. Craig, Surface roughness and hydrodynamic boundary slip of a Newtonian fluid in a completely wetting system, Phys. Rev. Lett. 9014 (14) (2003), 4501, art. no. 144501.
[13] N. Ishida, T. Inoue, N. Miyahara, K. Higashitani, Nano bubbles on a hydrophobic surface in water observed by tapping-mode atomic force microscopy, Langmuir 16 (16) (2000) 6377–6380.
[14] J.W.G. Tyrrell, P. Attard, Images of nanobubbles on hydrophobic surfaces and their interactions, Phys. Rev. Lett. 8717 (17) (2001) 6104++, art. no. 176104.
[15] R. Steitz, T. Gutberlet, T. Hauss, B. Klosgen, R. Krastev, S. Schemmel, A.C. Simonsen, G.H. Findenegg, Nanobubbles and their precursor layer at the interface of water against a hydrophobic substrate, Langmuir 19 (6) (2003) 2409–2418.
[16] Z.L. Guo, T.S. Zhao, S. Yong, Temperature dependence of the velocity boundary condition for nanoscale fluid flows, Phys. Rev. E 72 (2005), art no. 036301.
[17] P.A. Thompson, S.M. Troian, A general boundary condition for liquid flow at solid surface, Nature 389 (1997) 360–362.
[18] J.L. Barrat, L. Bocquet, Large slip effect at a nonwetting fluid–solid interface, Phys. Rev. Lett. 82 (23) (1999) 4671–4674.
[19] M. Cieplak, J. Koplik, J.R. Banavar, Boundary conditions at a fluid–solid interface, Phys. Rev. Lett. 86 (5) (2001) 803–806.
[20] V.P. Sokhan, D. Nicholson, N. Quirke, Fluid flow in nanopores: accurate boundary conditions for carbon nanotubes, J. Chem. Phys. 117 (18) (2002) 8531–8539.
[21] J.L. Xu, Z.Q. Zhou, X.D. Xu, Molecular dynamics simulation of micro-Poiseuille flow for liquid argon in nanoscale, Int. J. Numer. Methods Heat Fluid Flow 14 (5) (2004) 664–688.
[22] N.G. Hadjiconstantinou, Hybrid atomistic-continuum formulations and the moving contact-line problem, J. Comput. Phys. 154 (2) (1999) 245–265.
[23] R. Delgado-Buscalioni, P.V. Coveney, Continuum-particle hybrid coupling for mass, momentum, and energy transfers in unsteady fluid flows, Phys. Rev. E 6704 (4) (2003) 6704.
[24] P. Koumoutaskos, Multiscale flow simulations using particles, Annu. Rev. Fluid Mech. 37 (2005) 457–484.
[25] R. Delgado-Buscalioni, P.V. Coveney, USER: an algorithm for particle insertion in dense fluids, J. Chem. Phys. 119 (2) (2003) 978–987.
[26] X.D. Din, E.E. Michaelides, Kinetic theory and molecular dynamics simulations of microscopic flows, Phys. Fluids 9 (12) (1997) 3915–3925.